# Investigation of the impact of threshold pressure gradient on gas production from hydrate deposits

Cheng Lu[1,2,3,4], Xuwen Qin[2,5], Chao Ma[1,2 *], Lu Yu[1,2*], Lantao Geng[1,2], Hang Bian[2,4], Keni Zhang[6], Yingfang Zhou[7*]

1 Guangzhou Marine Geological Survey, China Geological Survey, Guangzhou 510760, China

2 Southern Marine Science and Engineering Guangdong Laboratory (Guangzhou), Guangzhou 511458, China

3 Center of Oil & Natural Gas Resource Exploration, China Geological Survey, Beijing 100083, China

4 School of Energy Resources, China University of Geosciences, Beijing 100083, China

5 China Geological Survey, Beijing 100083, China

6 Institute of Groundwater and Earth Sciences, Jinan University, Guangzhou, 510632, China

7 School of Engineering, University of Aberdeen, AB24 3UE, Aberdeen

[*] Corresponding author

**Abstract**

Many hydrate-bearing sediments are featured with unconsolidated argillaceous siltstones, which exist the non-Newtonian flow and threshold pressure gradient due to the high content of clay. In this study, the threshold pressure gradient of hydrate reservoir in the South China Sea is experimentally clarified. The quantitative relationship between it and the reservoir parameters is established. The function of threshold pressure gradient has been added into TOUGH+HYDRATE simulator. Here, site SH2, a candidate for field testing comprising a clayey silt gas hydrate reservoir in the Shenhu area of the South China Sea, was chosen to investigate the effect of threshold pressure gradient on gas production behavior through numerical simulations. The simulation results show that threshold pressure gradient has a significant impact on gas extraction. When the experimental value was applied, the gas production was enhanced unexpectedly, where cumulative gas output doubled in 5 years. The active hydrate dissociating area (gas, water and hydrate coexist) has notably extended, accompanying with the expanding cool zone. Water blockage near well was relieved.

However, with the increasing of threshold pressure gradient, propagation of pressure would be restrained seriously. The pressure and hydrate of far-field formations stay "frozen". The bottom water invasion was weakened.

**Keywords**: natural gas hydrate; threshold pressure gradient; argillaceous siltstones; numerical simulation

## 1. Introduction

Gas hydrate are solid crystalline compounds, in which small gas molecules are lodged within the lattices of ice-like crystals. Natural gas hydrate deposits involve mainly $CH_4$, and vastly exists in the permafrost and subsea or deep ocean sediments [1]. Estimates of global hydrate reserves are very high and about $2 \times 10^{12}$ tons of oil equivalent, which is equivalent to twice that of all other fossil fuels combined [2].

Gas production from natural gas hydrate reservoirs can be initialized by changing the reservoir condition outside of the hydrate stability zone; the production strategies include hydrate dissociation through thermal stimulation [3], depressurization [4-6], chemical potential shift [7-8], and the combinations thereof [9]. Among these, depressurization and thermal stimulation are the most known approaches to extract gas from natural hydrate zones [10]. Recently, some enhanced gas recovery strategies have been proposed to improve gas production from hydrate formation [11], for example the CO2/N2 mixture has been injected in the field of North Slope of Alaska to obtain a higher methane recovery [12].

More recently, a gas production pilot testing had been successfully conducted in Shenhu area of the South China Sea operated by China Geological Survey, in which over $30 \times 10^4$ $sm^3$ natural gas had been extracted during 60 days, with methane content up to 99.5% [13]. Furthermore, the second production test was progressed successively in March 2020 and achieved continuous gas production for 30 days, with a total gas output of $86.14 \times 10^4$ $sm^3$ [14]. According to the progress of natural gas hydrate exploration and test in South China Sea, there are still a lot of challenges and

uncertainties for a controllable and commercial gas extraction, including the high cost of offshore test and the complex multi-phase flow mechanism [15].

The studies of sedimentary features demonstrated that hydrate reservoirs in Shenhu area of the South China Sea are typical disperse type of hydrate accumulation, where hydrate is distributed in unconsolidated argillaceous siltstone (or fine-grained) sediments [16-20]. The sediment grain size analysis indicated that the content of coarse-grained sand was less than 10% and clayed silt was up to 90% [21]. The research suggests that the flow in sediments with high clay content usually exhibits non-Darcy behavior [22]. Clay particles in sediments are flaky and hydrophilic, with large specific area and high surface potential [23]. With the influence of micro-electric field, the bound water strongly attracted to the surface of clay particles has a solid-like property, which can cause great resistance to the water flow [24]. It is shown that, the pore water flow in fine-grained formations with high clay content departs further from the characterization of Navier-Stokes equation and appears as non-Newtonian phenomena [25]. It cannot conform to Darcy's law. The relationship of flow velocity and pressure gradient are nonlinear and there exists threshold pressure gradient (TPG). The existence of TPG in porous media with high clay content was proposed by Miller and Low [26]. Wu et al. [27] measured the threshold pressure of water phase for the high-salt argillaceous dolomite reservoir in Jianghan Basin. Wang et al. [28] showed that TPG is negatively correlated with permeability and positively correlated with water saturation based on the experiments and the relational fitted expression. Ren et al. [29] proposed the permeability is the main controlling reason of the TPG, and obtained the power function relationship between the TPG and the core permeability.

The hydrate reservoirs in the Shenhu area of the South China Sea are also typical reservoirs with high argillaceous content and low permeability. Liu et al. [30] found non-Darcy flow and TPG in the water phase seepage experiment of hydrate argillaceous siltstone core in the South China Sea. He shows that pore water flows only when the pressure gradient is greater than the minimum threshold pressure

gradient. Thus, it is necessary to find out the relations of TPG and flow conditions in the argillaceous silt hydrate reservoirs in the South China Sea and further apply it to hydrate exploitation. It is generally known that TPG can notably delay the change of fluid velocity during the exploitation of low-permeability reservoirs, which restricts the pressure propagation and thus accelerate water invasion at the later stage of exploitation [31]. Ning et al. analyzed the simulation results of Sulige tight gas field and discovered that the cumulative gas production would reduce by 16.7% under the influence of TPG [32].

At present, there have been many numerical simulation studies targeting at hydrate reservoirs in the China South Sea [33-37]. With the geological data at the first offshore gas hydrate production test site, Sun et al. [38] built a 2D numerical simulation model and investigated the short- and long-term production behavior of the hydrate reservoir in Shenhu area. Qin et al. [6] focused on the detailed response of the temperature and pressure in the first hydrate test in South China Sea. Yang et al. [39] emphasized the effect of the flow capability of overlying and underlying strata on hydrate production behaviors in depressurization-induced production of three-phase hydrate deposits using a horizontal well, based on the geological data at the second offshore gas hydrate production test site. Most of the scholars use TOUGH+HYDRATE simulator in their research. This code was developed by the Lawrence Berkeley National Laboratory, it can model the non-isothermal hydration reaction, phase behavior, flow of fluids and heat under conditions typical of natural gas hydrate deposits in complex formations. The model can handle any combination of the possible hydrate dissociation mechanisms (i.e., depressurization, thermal stimulation, and inhibitor-induced effects) [40]. However, none of the studies and simulators has discussed the TPG existing in low-permeability hydrate reservoirs in the South China Sea.

Therefore, in order to explore the characteristic of TPG in argillaceous silt hydrate reservoirs in the South China Sea and its influence on the evolution of

temperature, pressure and fluid saturation during the exploitation, this study coupled the multi-phase heat and mass transfer model, based on TOUGH+HYDRATE, with the newly developed TPG mathematic model. The conservation equations have been modified and the TPG module was added to TOUGH+HYDRATE, where the TPG experimental result of target hydrate-bearing sediment in China South Sea was used. A two-dimensional reservoir-scale production model based on the field data of SH2 drilling site was established for simulation. Meanwhile, the influence of TPG on the spatial distribution of the main physical fields and the evolution of gas production under depressurization were comparatively analyzed in detail.

## 2. Threshold pressure gradient model

### 2.1. Experiment setup

There exists a low velocity non-Darcy flow in the porous media with a high mud content [40]. The threshold pressure gradient can characterize this phenomenon concisely. In this study, the sediment sample obtained from pressure core of hydrate reservoir in Shenhu area of the South China Sea was used in the flow experiment in order to precisely quantify the TPG in argillaceous silt sediments.. Distilled water combined with 3.5 wt% *NaCl* was used throughout the experiments to simulate seawater. The experiment was carried out under room temperature. The schematic diagram of the experimental apparatus for TPG measurement is shown in Fig. 1. Through experimental fitting, the TPG of hydrate reservoir in the South China Sea is clarified and the quantitative relationship between the TPG and the reservoir parameters is established.

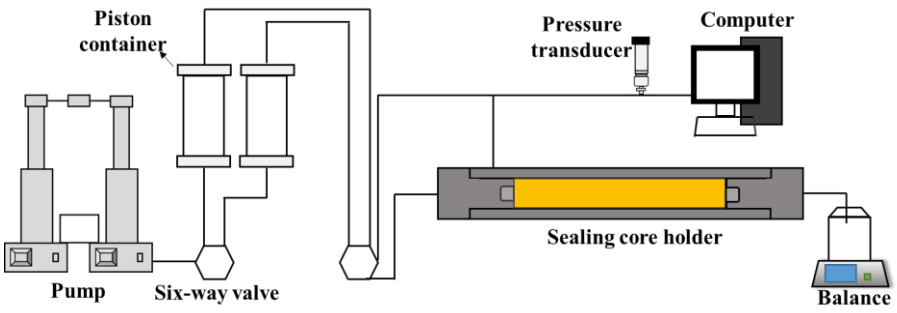


**Fig. 1 Schematic diagram of the threshold pressure gradient experiment process**

This experimental method innovatively combines the improved micro flow method with the steady-state method. A group of cores can first measure the minimum threshold pressure gradient, and then continue to measure the quasi-threshold pressure gradient with the steady-state method. Thus, the minimum threshold pressure gradient and the quasi-threshold pressure gradient can be measured on one core at the same time, and the comparison and optimization of the two threshold pressure gradients are realized. By using the experimental method of combining the improved micro flow method with the steady-state method, a total of 26 groups of experimental tests of 13 cores were completed.

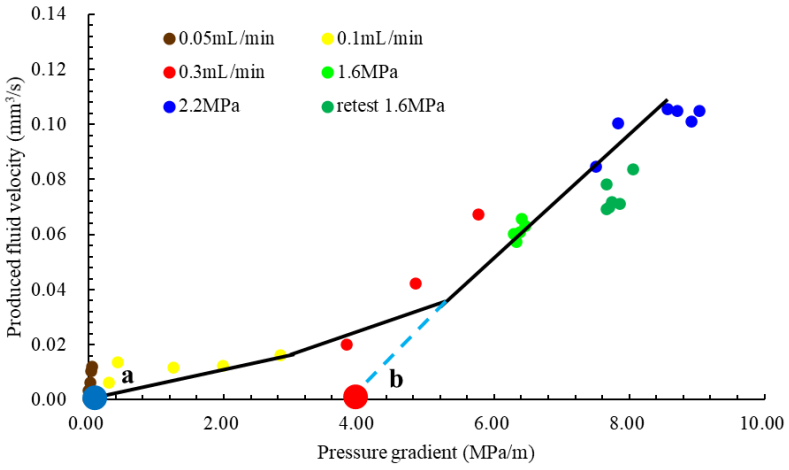


**Fig. 2 The relationship between the pressure gradient and the liquid production rate of the core BC08B-1-2**

Take the test data of core BC08b-1-2 as an example, we draw the relationship curve between pressure gradient and liquid production rate during core displacement, as shown in Fig. 2. According to the test principle of micro flow method, the corresponding pressure gradient at the moment before liquid outlet at the core outlet is the minimum threshold pressure gradient, that is, the pressure gradient corresponding to the starting point of pressure gradient and liquid production velocity curve is the minimum threshold pressure gradient. According to the test principle of steady-state method, on the relationship curve between pressure gradient and liquid production velocity, the straight-line section of the extended stable non-Darcy seepage curve

intersects with the coordinate axis, and the intersection point is the quasi-threshold pressure gradient. Therefore, it can be seen from the analysis of Fig. 2 that the minimum threshold pressure gradient of BC08b-1-2 core is 0.026 MPa/m (point **a** in the figure corresponds to the pressure gradient), and the quasi-threshold pressure gradient is 4.00 MPa/m (point **b** in the figure corresponds to the pressure gradient). In our experiment, the produced fluid was measured by electron balance method, and the accuracy is 0.01 g. Due to micro flow and steady-state displacement, the error of minimum threshold pressure gradient and quasi-threshold pressure gradient depend on the accuracy of the pressure sensor, which is 0.001 MPa for the measurement range of 0-5 MPa.

Using the above data analysis method, the minimum threshold pressure gradient and quasi-threshold pressure gradient corresponding to 13 core displacement experiments are obtained, as shown in Table 1. Take core BC08b-1-2 as an example, steady-state data of 1.6 MPa and 2.2 MPa (small blue points and green points) are used to calculated the permeability, and the average absolute deviation we evaluated is 1.63%. Our experiments also showed that: 1) the higher the confining pressure applied to the core, the lower the permeability $K$ value obtained from the test, which reflects that the higher the internal compaction degree of the core, the denser the core, and the worse the seepage capacity; 2) The average value of the minimum threshold pressure gradient of the core is 3.95 MPa/m, while the average value of the quasi-threshold pressure of the core is 15.4 MPa/m, and the quasi-threshold pressure gradient is about 4 times of the minimum threshold pressure gradient, which reflects that the threshold pressure gradients obtained by the two test methods are quite different. At present, the numerical range of the commonly used quasi-threshold pressure gradient is high, and the minimum threshold pressure gradient reflects the lower limit of the effective pressure gradient at both ends of the core when the fluid in the core begins to flow. Compared with the quasi-threshold pressure gradient, its physical significance and numerical range are more consistent with the actual

production situation. It is suggested to select reasonable threshold pressure gradient data according to the actual production situation.

**Table 1 The minimum threshold pressure gradient and quasi-threshold pressure gradient of different cores**

| Core number | *K* (mD) | Minimum threshold pressure gradient (MPa/m) | Quasi-threshold pressure gradient (MPa/m) |
|---|---|---|---|
| BC08B-1-2 | 0.0195 | 0.026 | 4 |
| BC08B-1-4 | 0.014 | 0.036 | 7.6 |
| BC08B-1-8 | 0.00335 | 3.61 | 15 |
| BC06B-1-2 | 0.0205 | 1.02 | 2.4 |
| BC06B-1-4 | 0.0122 | 2.55 | 6 |
| BC06B-1-8 | 0.00305 | 5.1 | 17 |
| BC06B-1-12 | 0.0021 | 11.9 | 20 |
| BC08B-2-8 | 0.0043 | 6.1 | 20 |
| BC08B-2-12 | 0.0025 | 8.3 | 32 |
| BC06B-2-2 | 0.00835 | 0.94 | 11 |
| BC06B-2-4 | 0.0068 | 3.1 | 12 |
| BC06B-2-8 | 0.0031 | 1.5 | 25 |
| BC06B-2-12 | 0.0018 | 7.2 | 28 |
| Mean value | | 3.95 | 15.4 |

The experimental results demonstrate that the relation of TPG and permeability-viscosity ratio presents a power function. Using power function regression analysis, the relationship equation between the TPG and permeability-viscosity ratio in hydrate reservoir of the South China Sea can be established as

$$\lambda = 0.14\left(\frac{k}{\mu}\right)^{-0.86} \tag{1}$$

where $\lambda$ is the threshold pressure gradient, MPa•m$^{-1}$; $k$ is the permeability, $10^{-3}$μm$^2$; $\mu$ is viscosity of liquid, mPa•s.

2.2 Selection of flow equation

According to the research results, there are mainly four forms of the mathematical models used to characterize the non-linear flow with TPG, as listed below.

$$\vec{v} = a\left[\text{grad}P - \lambda\right] \tag{2}$$

$$\vec{v} = a\left[\text{grad}P - \lambda\right]^{b} \tag{3}$$

$$\vec{v} = a\left[\text{grad}P\right]^{2} + b \cdot \text{grad}P + c \tag{4}$$

$$\vec{v} = a\left[\text{grad}P - b\right] \tag{5}$$

where $\vec{v}$ is fluid flow velocity, cm/s; grad$P$ is pressure gradient, $10^{-4}$ MPa/m; $a$, $b$, $c$ are regression coefficients of equation.

Among them, Eq. (2) is well consonant with the experimental observation, and can better reflect the nonlinear flow characteristics with TPG. In the establishment of flow equation, Bingham plastic fluid simulation method has been used for calculation. We can still use Darcy's law to describe its flow process by using the effective potential gradient method [41], as shown in Eq. (6).

$$\begin{aligned} \vec{v} &= -\frac{k}{\mu}\left[1 - \frac{\lambda}{\left|\text{grad}p\right|}\right] \cdot \text{grad}p \qquad \left|\text{grad}p\right| > \lambda \\ \vec{v} &= 0 \qquad\qquad\qquad\qquad\qquad\quad \left|\text{grad}p\right| < \lambda \end{aligned} \tag{6}$$

where $k$ is the permeability, μm$^2$; $\mu$ is viscosity of liquid, mPa·s.

## 3. Simulator improvement

The motion equation coupled with threshold pressure gradient is the evolvement of classical Darcy's equation [42]. In particular, a series of research results based on it can effectively guide the exploitation of argillaceous silt hydrate reservoirs in the South China Sea. In order to establish a more reliable flow model for hydrate exploitation in argillaceous silt sediments, this part combined the previously developed multi-phase flow equation and new TPG experimental model.

### 3.1 Conservation equation modification

Based on the TOUGH+HYDRATRE code, the general formula for mass and heat balance considerations is described as [43]

226 $$\frac{\mathrm{d}}{\mathrm{d}t}\int_{V_n} M^{\kappa}\mathrm{d}V = \int_{\tau_n} F^{\kappa} n \mathrm{d}\tau_n + \int_{V_n} q^{\kappa}\mathrm{d}V \tag{7}$$

227 where $M^K$ is mass accumulation term of component； $K$ are different components (i.e.,
228 water, methane, and water-soluble inhibitors); $F^K$ is flux vector of component; $q^K$ is
229 source/sink term of component.

230 The mass fluxes of water, $CH_4$ and inhibitor include contributions from the
231 aqueous and gaseous phases, i.e.,

232 $$F^{\kappa} = \sum_{\beta=A,\ G} F_{\beta}^{\kappa} \tag{8}$$

233 For the aqueous phase, the phase flux $\mathbf{F}_A$ is described by Darcy's law as:

234 $$F_A = -\frac{kk_{rA}\rho_A}{\mu_A} X_A^{\kappa}\left(\nabla P_A - \lambda\right) \tag{9}$$

235 where $k$ is absolute permeability; $k_{rA}$ are relative permeability of liquid phase; $\mu_A$ are
236 viscosity of the liquid phase; $P_A$ is aqueous pressure; $X^K{}_A$ is mass fraction of
237 component $K$ in liquid phase; $\lambda$ is threshold pressure gradient.

238 Considering that the gaseous flow would not be affected by TPG, the relevant
239 modification aimed to flux vector of component in liquid phase.

240 Among them, the mass conservation equation of water $w$ can be given by

241 $$\begin{aligned}&\int \frac{\partial}{\partial t}\left(\phi S_A \rho_A X_A^w + \phi S_I \rho_I + \phi S_G \rho_G X_G^w + \phi S_H \rho_H X_H^w\right) = X_A^w q_A + X_G^w q_G \\ &+\nabla\cdot\left[\frac{kk_{rA}\rho_A X_A^w}{\mu_A}\left(\nabla P_A - \lambda\right) + \frac{kk_{rG}\rho_G X_G^w}{\mu_G}\left(\nabla P_G\right)\right]\end{aligned} \tag{10}$$

242 where subscript $A$ represents liquid phase; subscript $I$ represents ice phase; subscript
243 $G$ represents gas phase; $\phi$ is porosity; $S_\alpha$ is saturation of phase $\alpha$; $\rho_\alpha$ is density of
244 phase $\alpha$; $X^w{}_\alpha$ is mass fraction of component $w$ in phase $\alpha$; $q_A$ is mass of productive
245 liquid phase; $q_G$ is mass of productive gaseous phase; $Q^w$ is mass of hydrate-related
246 release of water; $k$ is absolute permeability; $k_{rA}$, $k_{rG}$ are relative permeability of
247 liquid and gaseous phase; $\mu_A$, $\mu_G$ are viscosity of the liquid and gaseous phase; $P_A$ and
248 $P_G$ are aqueous pressure and partial methane pressure, respectively; $\lambda$ is threshold
249 pressure gradient.

The mass conservation equation of methane *m* in liquid phase can be defined as

$$\int \frac{\partial}{\partial t}\left(\phi S_A \rho_A X_A^m + \phi S_G \rho_G X_G^m + \phi S_H \rho_H X_H^m\right) = X_G^m q_G + X_A^m q_A + \nabla \cdot \left[\frac{k k_{rA} \rho_A X_A^m}{\mu_A}\left(\nabla P_A - \lambda\right) + \frac{k k_{rG} \rho_G X_G^m}{\mu_G}\left(\nabla P_G\right)\right] \tag{11}$$

where $X^m{}_\alpha$ is mass fraction of component *m* in phase $\alpha$； $Q^m$ is mass of hydrate-related release of methane.

The mass conservation equation of water-soluble inhibitor *i* in liquid phase can be expressed as

$$\int \frac{\partial}{\partial t}\left(\phi S_A \rho_A X_A^i\right) = \nabla \cdot \left[\frac{k k_{rA} \rho_A X_A^i}{\mu_A}\left(\nabla P_A - \lambda\right)\right] + X_A^i q_A \tag{12}$$

where $X^i{}_A$ is mass fraction of water-soluble inhibitors *i* in liquid phase.

These components are partitioned among four possible phases: gas phase, liquid phase, ice phase and hydrate phase. The hydrate in the reservoir turns into liquid phase and gas phase at the phase transition condition, and ice might be formed at subzero temperatures due to the endothermic effect of hydrate dissociation.

Considering the threshold pressure gradient, the heat conservation equation can be given by

$$\int \frac{\partial}{\partial t}\left[\left(1-\phi\right)\rho_R C_R T + \phi S_A \rho_A U_A + \phi S_G \rho_G U_G + \phi S_H \rho_H U_H\right] = Q_{diss} + \nabla \cdot \left[\left(1-\phi\right)K_R + \phi\left(S_A K_A + S_G K_G + S_H K_H\right)\right]\nabla T + \nabla \cdot \left[h_A \frac{k k_{rA} \rho_A}{\mu_A}\left(\nabla P_A - \lambda\right) + h_G \frac{k k_{rG} \rho_G}{\mu_G}\left(\nabla P_G\right)\right] \tag{13}$$

where subscript R represents rock matrix; $C_R$ is heat capacity of the dry rock; $U_\alpha$ is specific internal energy of phase $\alpha$; $Q_{\text{diss}}$ is equilibrium dissociation heat; $K_R$ is thermal conductivity of the rock matrix; $K_\alpha$ is thermal conductivity of phase $\alpha$; $h_A$, $h_G$ is the specific enthalpy of liquid and gaseous phase; *T* is temperature.

3.2 Threshold pressure gradient module

It can be revealed from the flow experiment that the threshold pressure gradient increases with the permeability of clayed sediment decreasing. When the permeability

is relatively high, the TPG increases slowly as the permeability decreases. When the permeability is relatively low, the TPG increases sharply as the permeability decreases. The TPG and the permeability-viscosity ratio agree with the power function. Therefore, the relationship between TPG and the permeability-viscosity ratio has been characterized through the power function formula in the newly-added TPG module.

$$\lambda = a\left(\frac{k}{\mu}\right)^{b} \tag{14}$$

where *a*, *b* are feature parameters， *b* is usually negative. Parameter *a* can control the dimension of TPG and *b* can determine the relationship between the TPG and reservoir parameters. Enter the values of *a* and *b* in this module and a specific TPG curve can be given.

Experimental values ($a$ = 0.14 and $b$ = −0.86) were used in the subsequent simulation, which was more suitable and fitted in with the actual circumstances.

## 4. Model setup

### 4.1 Geological background

Shenhu area is in the middle of the northern slope of South China Sea and tectonically located in the Zhu II Depression, Pearl River Mouth Basin [44, 45]. This area has already become a large source of oil and natural gas. Numerical simulations in this study are based on gas hydrate reservoir at the site SH2. In 2007, gas hydrate samples were collected at the site SH2 during a scientific expedition conducted by the Guangzhou Marine Geological Survey [46, 47]. The hydrate-bearing deposits at drilling site SH2 are at a depth of 185-229 mbsf, with a porosity of 40% and an average permeability of 10 mD. The seafloor is at a water depth of 1235 m, with a temperature of 3.9°C. Hydrate saturation varies with depth. In situ measurements indicated that the highest hydrate saturation reached 47% and the average hydrate saturation was 16.5%. The gas produced from the hydrate consists of 96.1-99.82% methane.

### 4.2 Model construction

In this study, a synthetic multi-phase flow models with TPG described above was created with fundamental hydrate bearing sediments parameters collected from Shenhu area in the South China Sea. In order to focus on TPG effect analysis and minimize the influence from different aspects, the following assumptions have been made in the numerical model: the pure methane is generated from hydrate; the hydrate-bearing layers, overlying layers and underlying layers are homogenous, and the mechanical properties of hydrate sediment stay unaffected during hydrate dissociation process. In order to avoid the influence of grid size on the numerical simulation results, prior to this study, we have performed grid refinement study to find the desirable gride size. This information has now also been added in the revised manuscript.

As shown in Fig. 3, the hydrate reservoir model consists of the three basic layers: 44 m thick methane hydrate layer, two 30 m thick overlying and underlying formations with similar permeability conditions. It consists of 120 radial grid layers and 110 vertical grid layers, with a total grid layer quantity of 120 × 110 =13200. The grids of the methane hydrate layers and the near-wellbore area are refined in order to increase the accuracy of simulation.

The pressure and temperature at the bottom of the hydrate is calculated to be 15.22 MPa and 15.01 ℃. The top and bottom pressure are respectively 14.5 MPa and 15.47 MPa. The top and bottom temperature are respectively 11.75 ℃ and 16.21 ℃. The overburden and underlying layer are fully saturated with water. The main properties of the simulated hydrate bearing sediment are listed in Table 2 [48, 49].

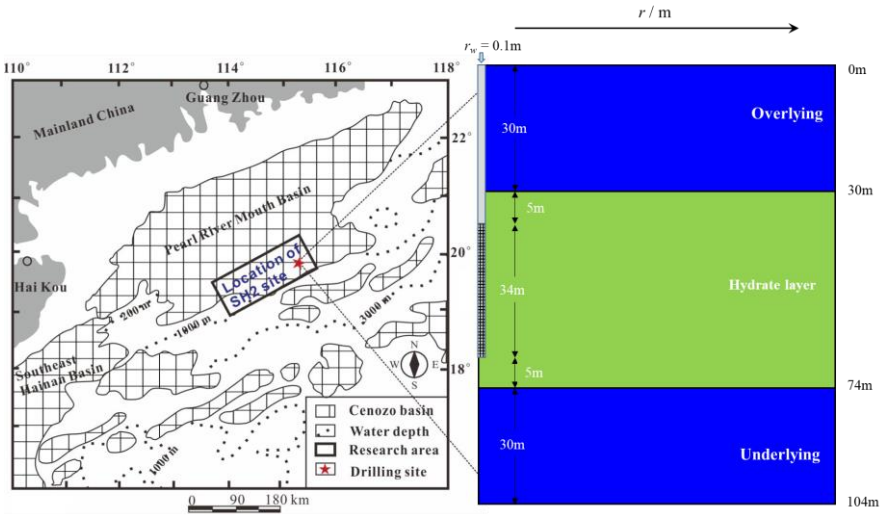


**Fig. 3 Schematic model of the methane hydrate production scenario**

**Table 2 Basic hydrate reservoir properties**

| Parameter | Value |
|---|---|
| Thickness of hydrate layer /m | 44 |
| Thickness of overburden layer /m | 30 |
| Thickness of underlying layer /m | 30 |
| Model radius /m | 1000 |
| Well radius /m | 0.1 |
| Permeability of overburden layer /mD | 10 |
| Permeability of hydrate layer /mD | 10 |
| Permeability of underlying layer /mD | 10 |
| Porosity of overburden layer | 0.42 |
| Porosity of hydrate and underlying layer | 0.4 |
| Initial hydrae saturation | 0.165 |
| Gas component | 100%$CH_4$ |
| Grain density (kg/m$^3$) | 2600 |
| Compression coefficient (Pa$^{-1}$) | $1.0\times10^{-8}$ |
| Wet thermal conductivity (W/m/K) | 3.1 |
| Relative permeability mode | $k_{rG} = \left(S_G^*\right)^n$ |

| | |
|---|---|
| | $k_{rA} = (S_A^*)^n$ |
| | $S_A^* = (S_A - S_{irA})/(1 - S_{irA})$ |
| | $S_G^* = (S_G - S_{irG})/(1 - S_{irA})$ |
| Capillary pressure model (van Genuchten Model) | $P_{cap} = -P_0\left(\left[S^*\right]^{-1/\nu} - 1\right)^{1-\nu}$ |
| | $S^* = (S_A - S_{irA})/(S_{mxA} - S_{irA})$ |

Where $k_{rG}$, $k_{rA}$ are relative permeability of gaseous and liquid phase; $S_G$, $S_A$ are saturation of gaseous and liquid phase; $S_{irG}$, $S_{irA}$ are the irreducible gas and water; $P_{cap}$ is capillary pressure; $P_0 = 10^5$ Pa; $S_{mxA} = 1 - S_{irG}$ is maximum water saturation; $\nu$ is van Genuchten exponent.

4.3 Well design

A vertical well with a diameter of 0.1 m was drilled for hydrate exploitation by depressurization. The perforation section is 34 m (−35 m to −69 m in the model). The production well is operated at a constant pressure of 4.5 MPa at bottom of the wellbore. The production period is 5 years.

## 5. Result and analysis

5.1 Production behavior

The simulation results of the cases applying TPG and no TPG are compared with each other in this part. Fig. 4 shows the comparison of gas and water production within 5 years. It can be seen from Fig. 4a that, when the TPG is not applied, gas production rate drops quickly from the peak value (> 3000 $sm^3/d$) to 1266 $sm^3/d$ in the 200th day and the decreases slowly to less than 800 $sm^3/d$. When the TPG is applied, initial decline of gas production still exists but it only drops to 1580 $sm^3/d$ in the 200th day. After that, the gas production rate begins to boom, which is absolutely different from the case without TPG. Of interest is the increase at late times and the gas production rate climbed to 2732 $sm^3/d$ at the end. Fig. 4b reveals that, when the TPG is not applied, the cumulative gas production in 5 years is only $178.4 \times 10^4$ $sm^3$. While considering the TPG, the cumulative gas production reaches $382.1 \times 10^4$ $sm^3$,

which is more than twice of the former. TPG also makes a distinct impact on water production. Fig. 4c demonstrates that, without TPG, the water production rate fluctuates at a stable and slowly increasing state in a long term. As production progresses, water saturation in the reservoir increases, resulting in increased water production rates in the later stage, which increases from 320 $m^3$/d at initial to 370 $m^3$/d at the end. However, when TPG is applied, the water flow seems to be restrained. The water production reduces gradually to 68 $m^3$/d and the cumulative water production is only 18.2 × $10^4$ $m^3$, which is much lower than that without TPG (63.4 × $10^4$ $m^3$).

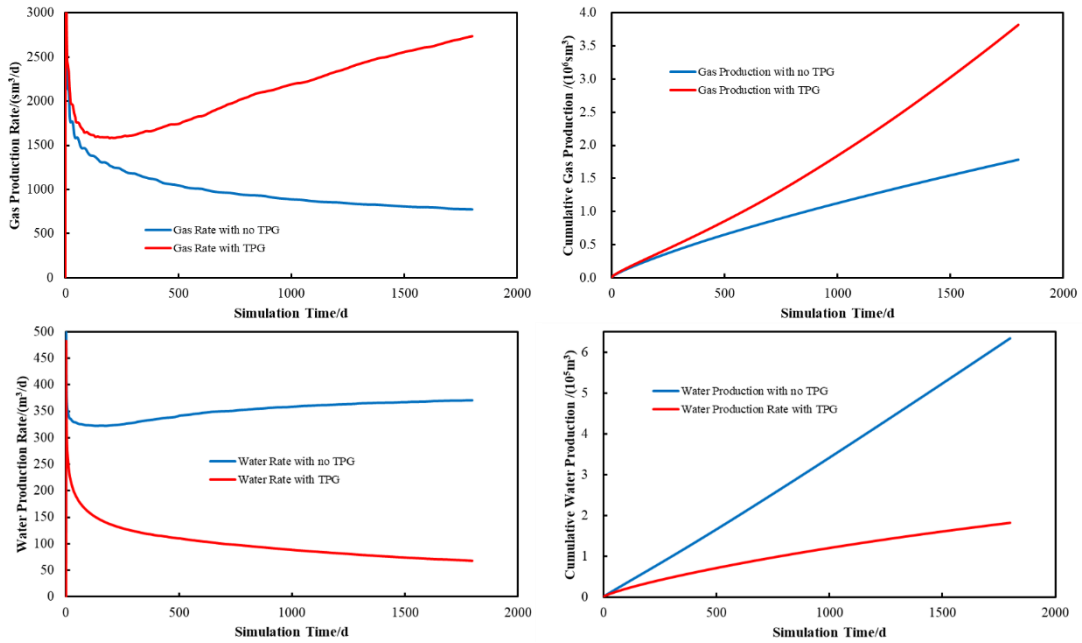


**Fig. 4 Performance of fluid productions applying TPG and no TPG**

Note that while a reduction in water production is expected because the threshold pressure can delay the pressure propagation, the evolution of gas output is contrary to expectation. It can be preliminarily concluded that TPG in argillaceous silt reservoir derived from flow experiment is propitious to enhance recovery. As quantified in Fig. 5, the gas-water ratio with TPG gradually increases and can exceed 40 by the end of the simulation. In contrast, the gas-water ratio without TPG is close to 2. A too low gas-water ratio may cause difficulties to downhole gas-water separation, which is extremely unfavorable in practice.

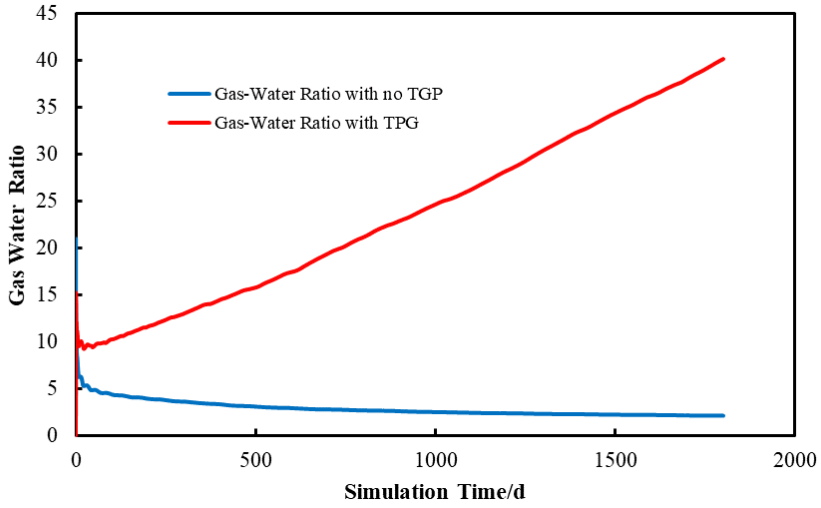


**Fig. 5 Performance of Gas-water ratios applying TPG and no TPG**

5.2 Evolution of reservoir parameters during production.

The reason for the influence of TPG on productivity can be further discussed by analyzing the continuous evolution of reservoir parameters during hydrate exploitation. The variations of the pressure, temperature and saturation during gas production are plotted in Fig. 6 to 10.

Review of the pressure profile in Fig. 6 shows the difference of pressure evolution caused by TPG. Fig. 6a, b and c reveal the distribution of pressure at the 50th, 500th, and 1800th day without TPG and Fig. 6d, e and f show those with TPG. Simulation results without TPG indicates that the pressure distribution conforms to expectations, as maximum pressure drops near the well and overall pressure decline in the reservoir over time. In Fig. 6c, pressure advance front looks approximately horizontal. Although the range of pressure drop is relatively larger, the degree of that is low. The front of pressure drop, which is larger than 10 MPa, advances less than 5 m. The most striking feature with TPG in Fig. 6d is the emergency of the radial extension of pressure advance front around the perforation section. While the pressure front reaches only 120 m, the pressures of underlying layer and overlying layer drop significantly and the front of the low-pressure area (< 10MPa) advances to 40 m, which is quite beneficial to the hydrate dissociation.

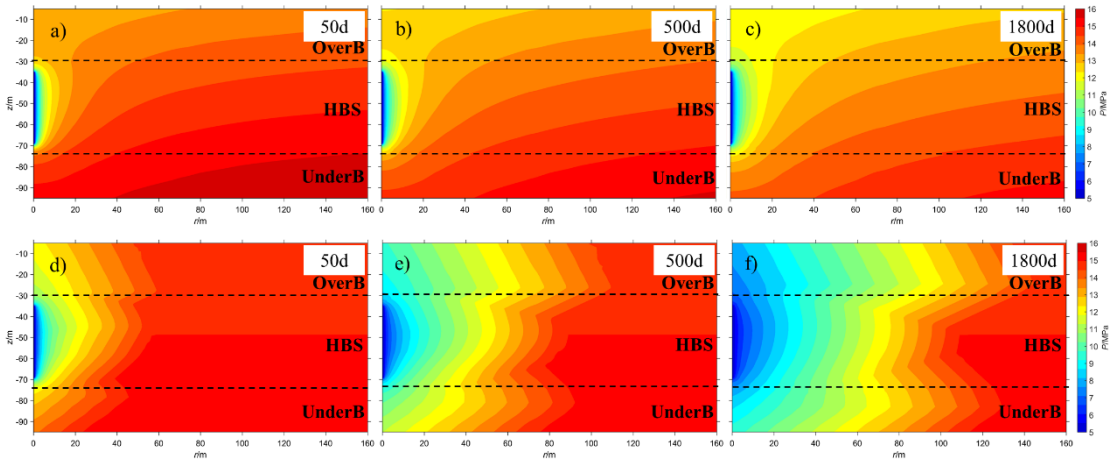


**Fig. 6 Effect of TPG on the pressure distribution (a-50d without TPG, b-500d without TPG, c- 1800d without TPG; d-50d with TPG, e-500d with TPG, f-1800d with TPG)**

Hydrate dissociation is a typical endothermic reaction. Review of the temperature profile in Fig. 7 can effectively reflect the dynamics of hydrate. Localized effects like the cooling in dissociating hydrate-bearing layers are easily recognizable. The expanding and sagging cool zones are caused by continuing dissociation, Joule-Thomson cooling, and drainage of the cooler water released from dissociation. Fig. 7a, b and c reveal the distribution of temperature at the 50th, 500th, and 1800th day without TPG and Fig. 7d, e and f show those with TPG. When TPG is not applied, the expanding colder zone adjacent to the overlying layer (< 12°C) appears within 1-3 m near the well in the early stage of production, as Fig. 7a confirm. Of interest is the shrinkage of the cool zone in the main hydrate body at 500d in Fig. 7b, when compared to that at 50d in Fig. 7a. It means that the amount of hydrate dissociating gradually decreases, which is consistent with the decline in gas production. Fig. 9c clearly shows that the bottom water intrusion from the underburned layer also brings about the temperature rise at the bottom of the production well. As depicted in Fig. 7d to 7f, considering TPG, the area with low temperature (< 12°C) in the initial stage of production reaches 10 m and gradually expands as time advances. By the end of the simulation, the front of the low-temperature region has extended to 50 m, it is shown that the rise of bottom water affects the fall of temperature.

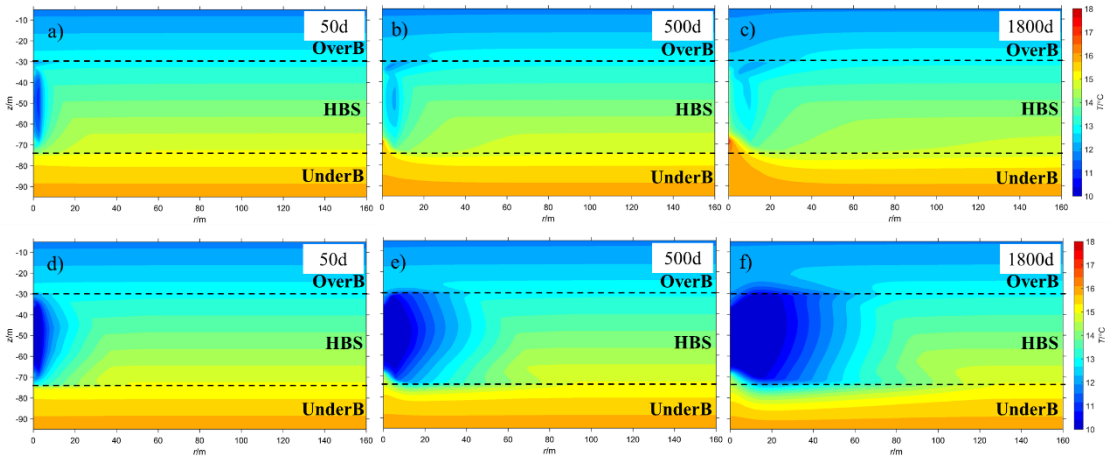


**Fig. 7 Effect of TPG on the temperature distribution (a-50d without TPG, b-500d without TPG, c- 1800d without TPG; d-50d with TPG, e-500d with TPG, f-1800d with TPG)**

Some of the most interesting observations can be made from the distribution of the hydrate saturation in Fig. 8. Fig. 8a, b and c reveal the distribution of hydrate saturation at the 50th, 500th, and 1800th day without TPG and Fig. 8d, e and f show those with TPG. From the comparison between results without and with TPG, it can be seen that there is little difference in the range of the hydrate dissociated area where only gas and water phases exist. When TPG is applied, the advance speed of the front of the active dissociation regions, which reaches 80 m from well, is much higher than that without TPG. Fig. 8f shows clear signs of the markedly lower hydrate saturation in active dissociation regions.

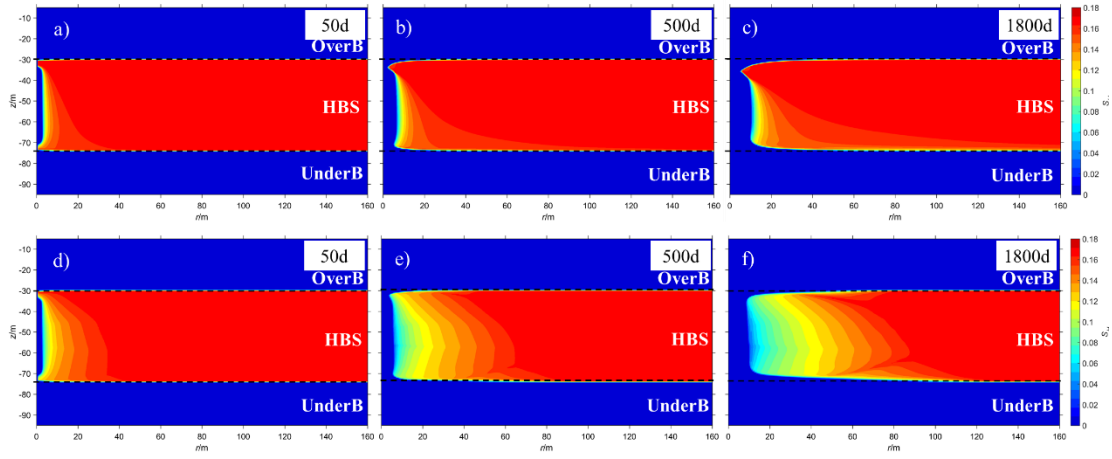


**Fig. 8 Effect of TPG on the hydrate distribution (a-50d without TPG, b-500d without TPG, c- 1800d without TPG; d-50d with TPG, e-500d with TPG, f-1800d with TPG)**

The TPG also has a great impact on the liquid and gaseous phase saturation. Fig. 9a, b and c reveal the distribution of water saturation at the 50th, 500th, and 1800th

day without TPG and Fig. 9d, e and f show those with TPG. Fig. 9c shows clear signs of the zone with high water saturation around the production well, probably causing "water blockage". In contrast, Fig. 9f shows the emergence of a slightly water-saturated zone around the well. In Fig. 9f, Aquifers invading into hydrate layer are smaller in volume than that in Fig. 9c. Bottom water invasion may cause the increase of water production rate in the late time of simulation without TPG.

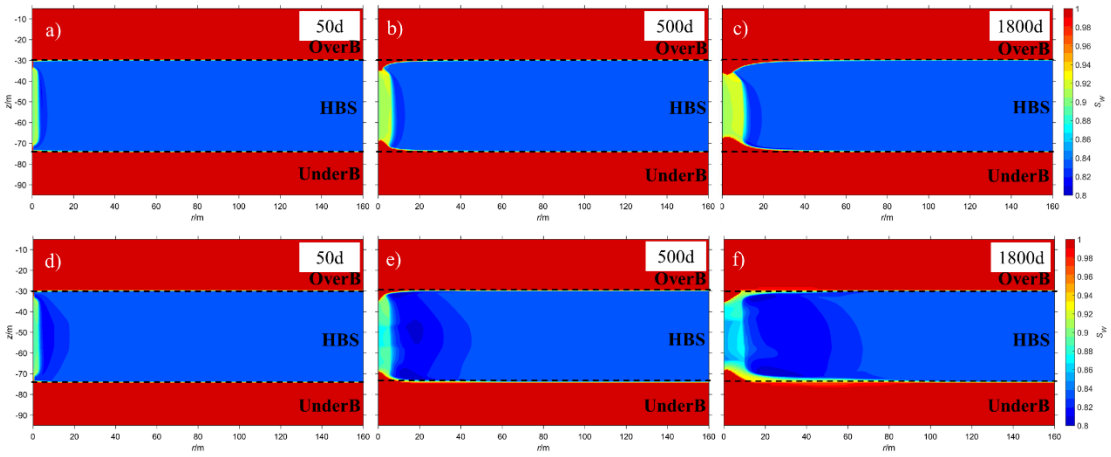


**Fig. 9 Effect of TPG on the aqueous phase distribution (a-50d without TPG, b-500d without TPG, c-1800d without TPG; d-50d with TPG, e-500d with TPG, f-1800d with TPG)**

The evolution of gaseous phase saturation distributions in the reservoir are shown in Fig. 10. Fig. 10a, b and c reveal the distribution of gaseous phase saturation at the 50th, 500th, and 1800th day without TPG and Fig. 10d, e and f show those with TPG. When TPG is not applied, the gas saturation conforms to expectations, with maximum enrichment near well. When TPG is applied, the gas enrichment near well is enhanced.

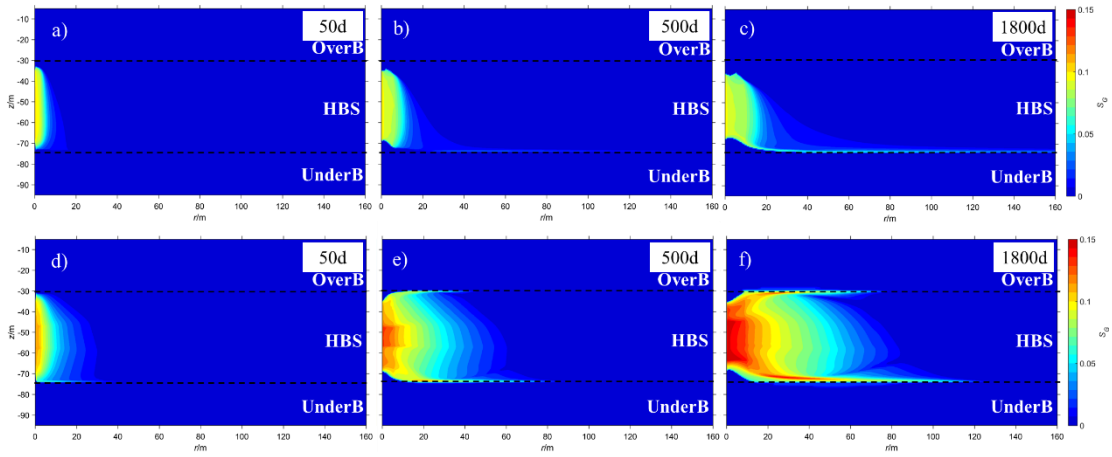

**Fig. 10 Effect of TPG on the gas phase distribution (a-50d without TPG, b-500d without TPG, c-1800d without TPG; d-50d with TPG, e-500d with TPG, f-1800d with TPG)**

5.3 Influence of different TPG on evolution of system conditions

In order to evaluate the influence of different TPGs on the evolution of system conditions during production, the feature parameters in Eq. (14) were set with different values. Table 3 shows the corresponding TPGs with different *a*.

**Table 3 Model parameters and the corresponding TPG**

| No. | Value of *a* | Corresponding TPG (MPa·m$^{-1}$) |
|---|---|---|
| case 1 | 0 | 0 |
| case 2 | 0.07 | 0.2542 |
| case 3 | 0.14 | 0.5083 |
| case 4 | 0.28 | 1.0166 |
| case 5 | 0.7 | 2.5415 |
| case 6 | 1.4 | 5.0831 |

Fig. 11 shows the gas production behavior with TPGs with a constant bottom-hole pressure (4.5 MPa). Under depressurization without TPG, it is illustrated that the gas production rate is relatively low and declines over time. The output result is optimal when $a$ = 0.28, and the TPG $\lambda$ = 1.0166 MPa/m, which is twice the experimental value. In this case, the gas production rate drops to 2129 sm$^3$/d on the 73rd day, then it gradually increases and stabilizes at 2700 sm$^3$/d about 800 days later. When the value of $a$ = 0.7 and $\lambda$ = 2.5415 MPa/m is used, the gas production rate (772 sm$^3$/d) is close to that of the case without TPG (664 sm$^3$/d) at the end of the simulation. However, when $a$ = 0.7, the initial gas production rate decreased slightly, and the production in the first 1000 days remained above 1000 sm$^3$/d. A larger $a$ in case 6 is expected to result in the obstacle for pressure propagation, and, consequently in insufficient hydrate dissociation. Consistent with expectations, the corresponding gas production has slipped, as a review of the simulation outputs indicates.

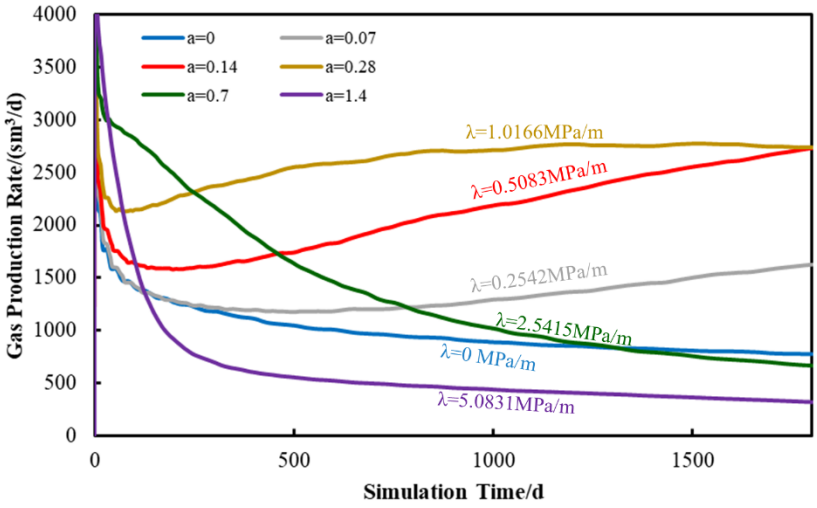


**Fig. 11 Comparison of gas production rate at different starting pressures**

The distribution of pressure, temperature on the 1800$^{th}$ day of production with different TGPs are depicted in Fig. 12.

As is a common occurrence in the case without TGP that the pressure drop spreads rapidly across the formation as time advances. From Fig. 12a, it can be seen that the pressure front can reach 150 m away. In the cases considering TPG by Eq. (14) with different *a*, the pressure distribution presents various patterns. It is mainly reflected in two aspects. Firstly, in the vertical direction, pressure advance front behaves as a radial extension. Secondly, in the lateral direction, the TPG acts like that it could make the pressure of far-field formations stay “frozen” and make the pressure drop only occur near the well. Comparing different graphs in Fig. 12a, an important observation is that the depressurization is faster near the well with a relatively small *a*, so hydrates can dissociate more efficiently and cooling is more pronounced at this location. However, when the TPG gradually increases, the lateral extension of the pressure drop is gradually blocked, making the hydrate far away from well hardly reach its equilibrium pressure. Especially when $a$ = 1.4 (6$^{th}$ graph in Fig. 12b), hydrate dissociating zone is limited within 20 m after 1800 days of production, with the shrinkage of progressive cooling zone caused by continuing dissociation.

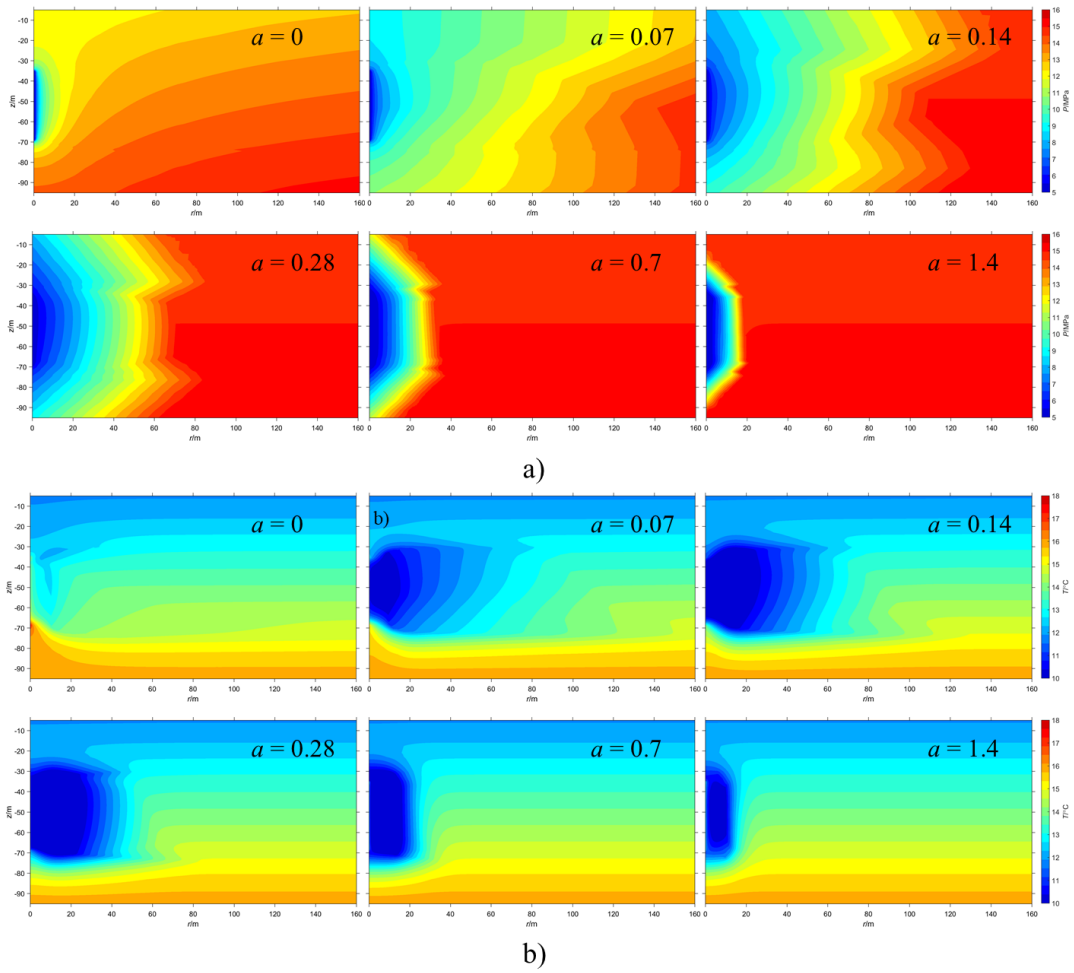


**Fig. 12. (a) Pressure distribution and (b) temperature distribution with different TPGs on the 1800$^{th}$ day.**

Fig. 13 show the pressure and temperature drop funnel (100 m away from the well, −60 m in the model) with different TPGs after 1800 days of production. It can be demonstrated from Fig. 13a that the radius of pressure drop funnel reduces with the increase of TPG. For the temperature drop funnel exhibited in Fig. 13b, the greater the TPG, the smaller the radius of funnel. However, by comparison of different graphs in Fig. 13b, the depth of temperature drops funnel augments firstly, then decreases with the rise of TPG. The minimum temperature in the profile is about 10 ℃ and occurs in the vicinity of the production well. It is a favorable situation that the temperature in the reservoir declines by 5 ℃ (from its original 15 ℃). That indicates that, under the conditions in this study, the temperature drops are mild and the risk of evolution of ice is minimal. For the presence of ice in the hydrate reservoirs may reduce the effective permeability or even block the flow path of the fluid phases to the proximity of the well, which will have a significant influence on gas production, especially for the gas

production in the short term [50, 51].

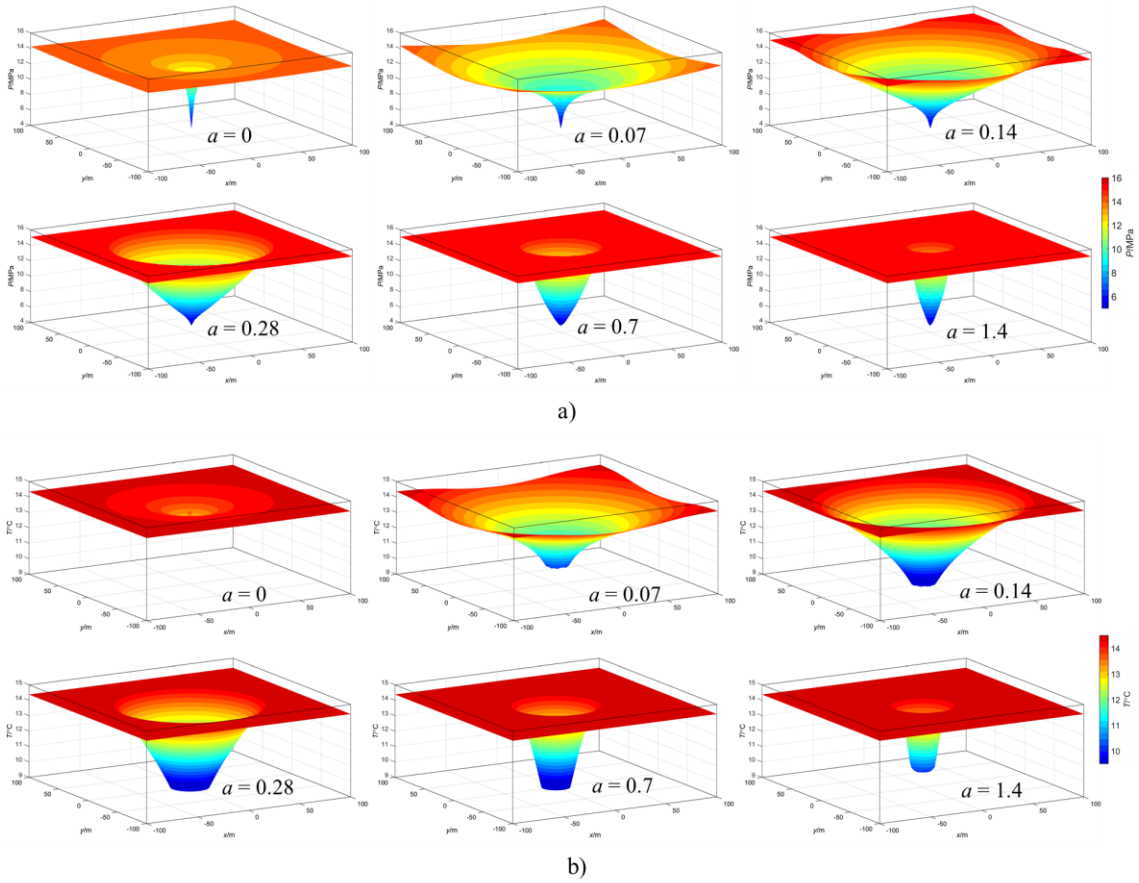


**Fig. 13. (a) The pressure drop funnel and (b) temperature drop funnel on the 1800th day with different TPGs.**

Fig. 14 show the distribution of hydrate saturation, liquid phase saturation and gaseous phase saturation after 1800 days of production with different TPGs. The front of hydrate dissociated zone without TPG is 15 m away from the well. When considering the TPG, the front of active dissociation regions in reservoir is greatly extended. That means the range of three-phase zone, where gas, water and hydrate coexist, expands remarkably. In 2$^{nd}$ graph of Fig. 14a, the hydrate active dissociation area has expanded to 110 m away from the well. However, with the TPG gradually increasing, the width of the three-phase zone is gradually reduced. There is almost no three-phase zone, as the 6$^{th}$ graph in Fig. 13a confirms.

As can be seen in Fig. 14b, there is a highly water-saturated region around the production well in the case without TPG. When the TPG is relatively small (Fig. 14b), the highly water-saturated region around the well disappears and is replaced by the gas-rich area (Fig. 14c). When the TPG continues to increase, the highly

water-saturated region reappears, but there is still a gas-rich area next to the well.

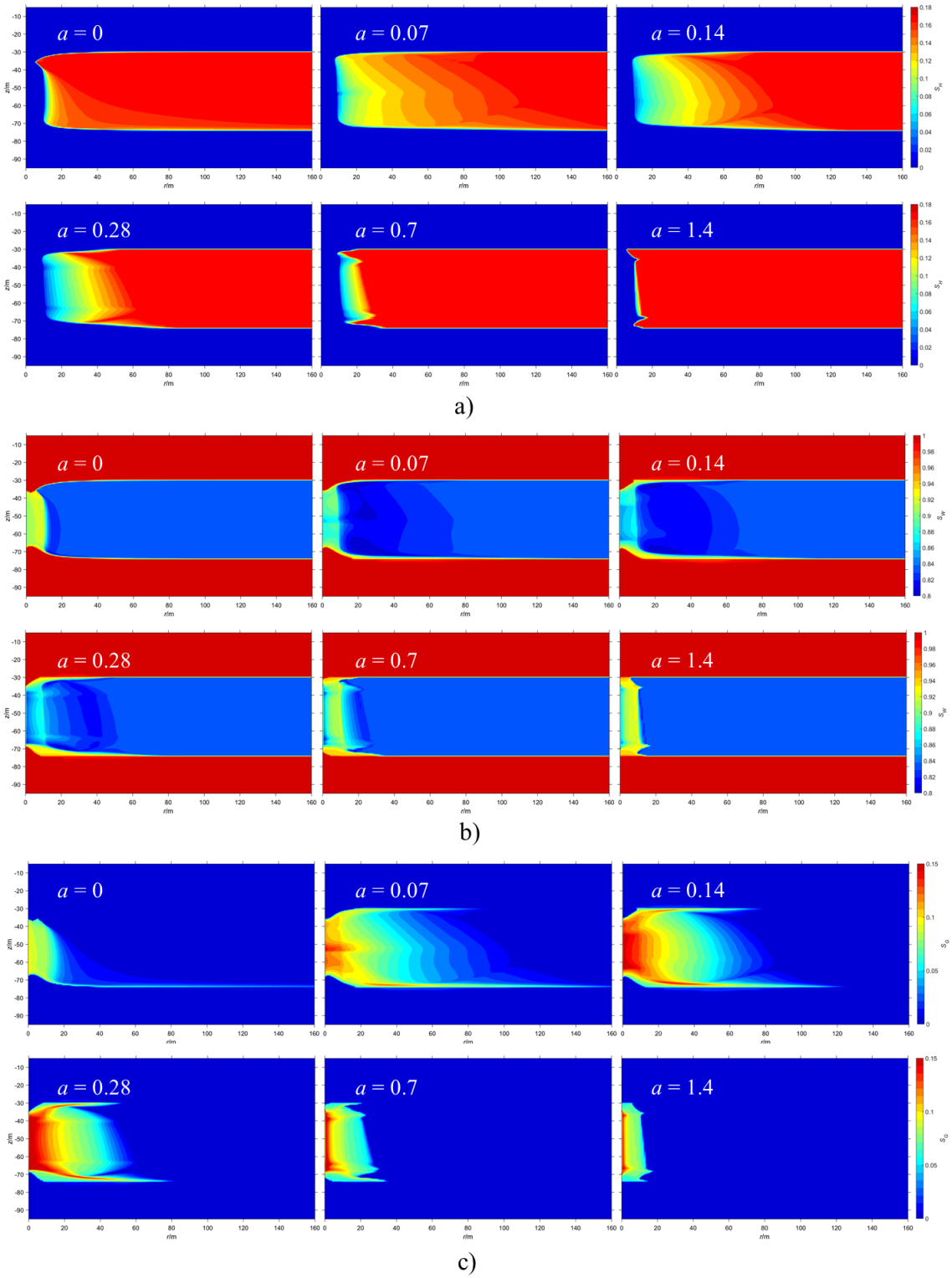


**Fig. 14. (a) Hydrate saturation distribution, (b) liquid phase saturation distribution and (c) gaseous phase saturation with different TPGs on the 1800$^{th}$ day.**

Because the production well did not completely penetrate the hydrate layer, the bottom water invasion appears in the results [52]. Fig. 15 shows the comparison of the

bottom water evolution under different TPGs. Fig. 16 shows the 3D patterns of bottom water evolution. The aquifer invading into hydrate layer is obvious in the case without TPG. On the 1800$^{th}$ day, the height of aquifer reaches 7 m and the radius of that exceeds 25 m. In Fig. 15b, the height of aquifer does not decrease significantly, but the radius reduces to about 16 m. With the TPG increases, the height of the invading aquifer gradually decreases and the radius also shrinks rapidly. The height in Fig. 15e has dropped to lower than 2 m and the radius has shrunk to smaller than 5 m. The invasion of bottom water has even disappeared, as Fig. 16f shows.

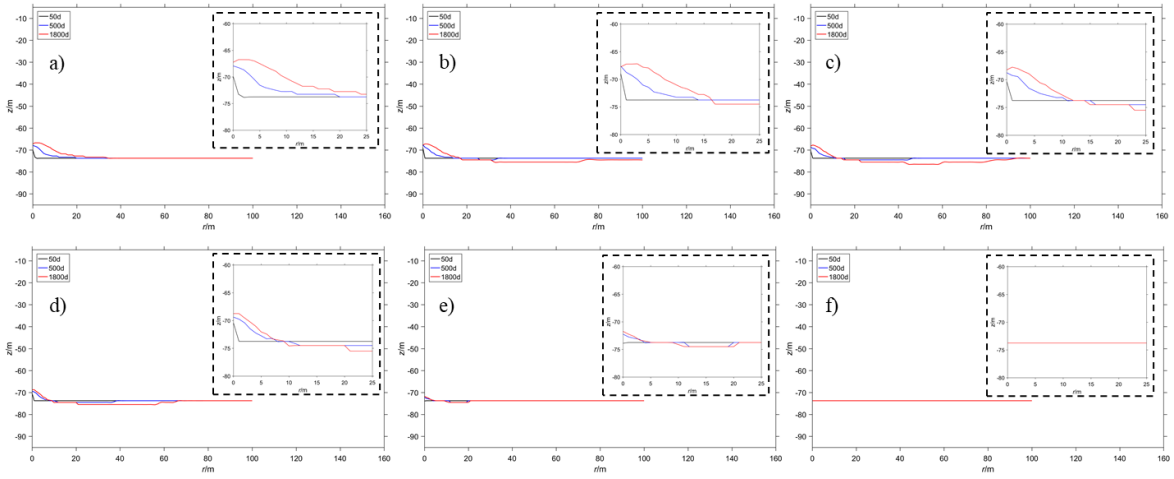


**Fig. 15. Comparison of bottom water invasion evolution under different TPGs, a) *a* = 0, b) *a* = 0.07, c) *a* = 0.14, d) *a* = 0.28, e) *a* = 0.7, f) *a* = 1.4.**

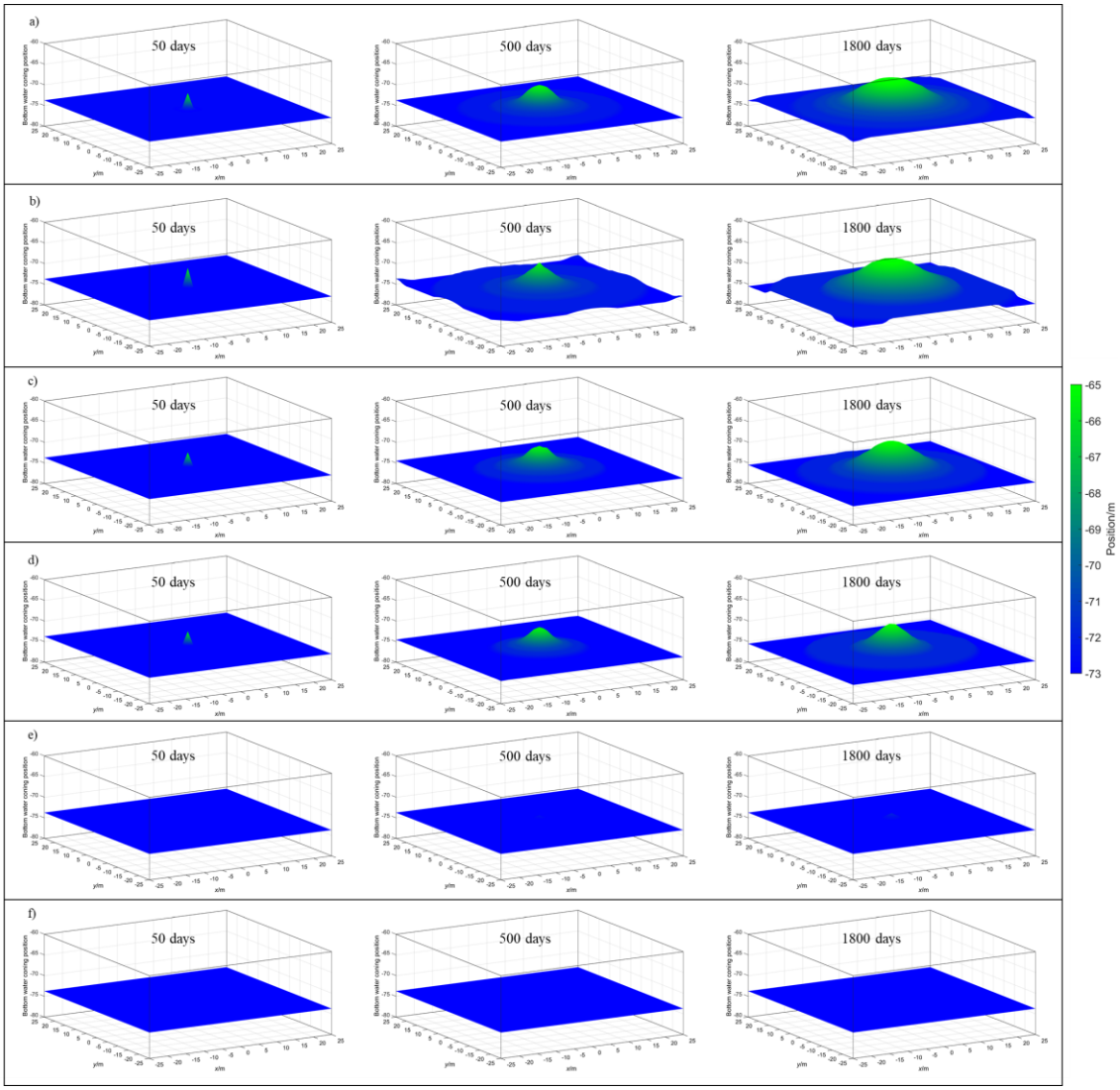


**Fig. 16. Comparison of 3D patterns of bottom water invasion evolution under different TPGs, a) $a$ = 0, b) $a$ = 0.07, c) $a$ = 0.14, d) $a$ = 0.28, e) $a$ = 0.7, f) $a$ = 1.4.**

Fig. 17a shows the advance front of the active dissociation region after 1800 days of production under different TPGs. The blank part is the area where the hydrate saturation is smaller than initial value. The larger the TPG, the smaller the blank part. Review of the simulation results from Fig. 17a indicates that the TPG plays a vital role in improving the recovery of hydrate in the upper part of the hydrate layer. Fig. 17b shows the advance front of the hydrate dissociated region after 1800 days of production under different TGPs. There is no hydrate in the blank area. Although the pressure, temperature, and saturation distribution of the reservoir are quite different under different TPGs, the width of hydrate dissociated region is roughly the same. The only difference lies at the interface of the hydrate layer and cover layer. As the TPG accelerates the pressure drop in the depressurization area, the hydrate at the

interface can completely dissociate in response to the sufficient heat supply from the upper and lower layers. As the active dissociation region is restricted by the heat supply, large area of hydrate cannot dissociation completely. Combining Fig. 17a and 17b, it can be seen that as the value of *a* increases, the distance between the front of dissociated area and that of active dissociation region becomes smaller and smaller.

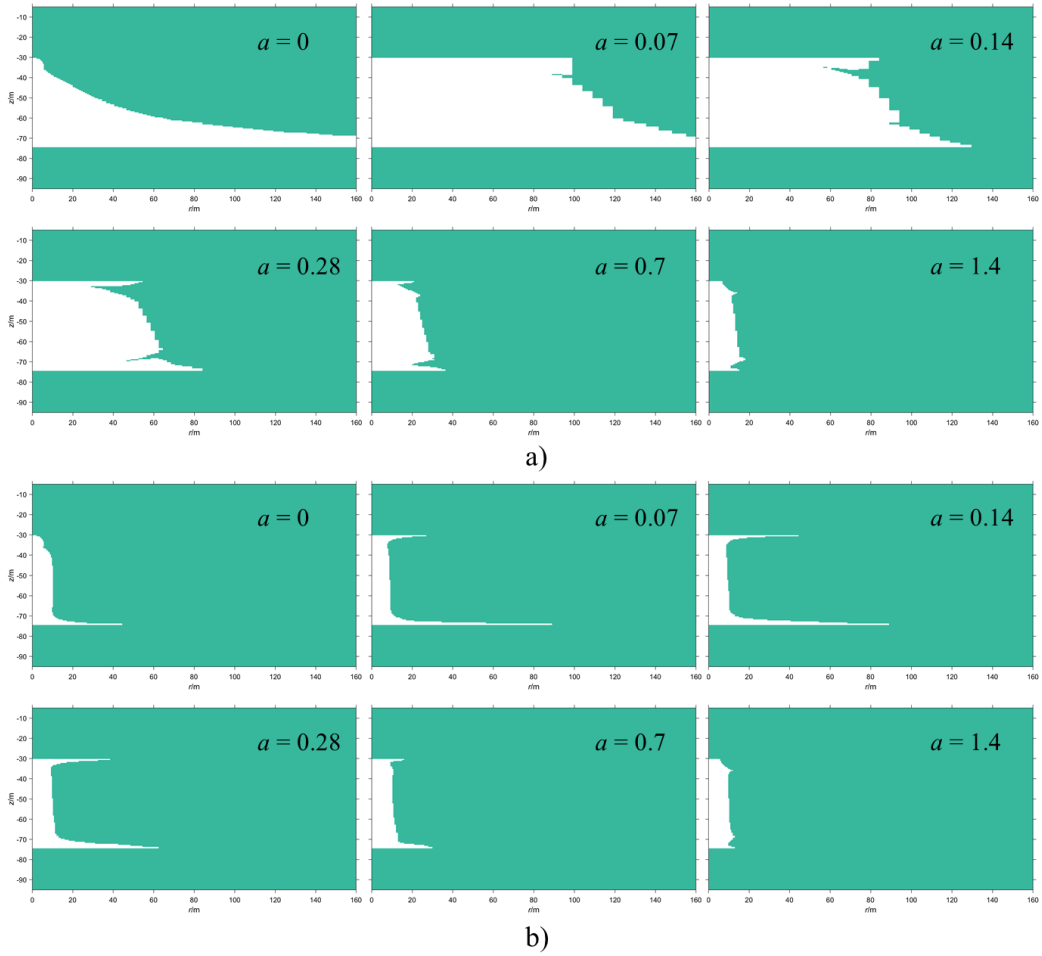


**Fig. 17 The front of (a) active dissociation region and (b) dissociated area after 1800 days under different TPGs, a) *a* = 0, b) *a* = 0.07, c) *a* = 0.14, d) *a* = 0.28, e) *a* = 0.7, f) *a* = 1.4.**

## 6. Conclusions

The following conclusions can be drawn from this study:

(1) The threshold pressure gradient in hydrate reservoir with argillaceous silt sediments has been quantified from the flow experiment. The TPG and the permeability-viscosity ratio agree with the power function.

(2) The conservation equations have been modified and the TPG module was added to TOUGH+HYDRATE, where the above result of target hydrate-bearing sediment in China South Sea was used. Running this function would increases time consumed.

(3) The TPG plays a critical role in gas production from hydrate-bearing sediments with unconsolidated argillaceous siltstones. When the TPG of experimental value is applied, targeting at hydrate reservoir at the site SH2, production capacity has been enhanced unexpectedly. It is responsible for progressive gas production rate, depressed water production and relatively great gas-water ratio. The pressure advance front behaves as a radial extension in the vertical direction, within which the pressure drop near well is stronger. Compared with that without TPG, the front of hydrate completely dissociated area has not moved forward. However, the active hydrate dissociating area (gas, water and hydrate coexist) has notably extended, which results in progressive cooling zone caused by continuing dissociation. Meanwhile, the TPG also contributes to a slightly water-saturated zone around the well, instead of a highly water-saturated zone that may cause water blockage.

(4) From the sensitivity analysis, the TPG with a small value can effectively expand the gas output, which can expand the three-phase coexisting area mentioned above. However, when the TPG further increases, propagation of pressure would be restrained seriously and the pressure drop only occurs near the well. It certainly accelerates the depressurization near the well, but the pressure and hydrate of far-field formations stay “frozen”. That means, with increasing gradually, the TPG converts from an assistance to an obstacle.

(5) When the production well does not completely drill out the hydrate layer, the bottom water invasion would appear. The TPG can restrict the aquifer invading into hydrate layer.

In this work, we first formatted the TPG model based on room temperature core flooding test and then investigated the influence of TPG on multi-phase seepage in

argillaceous siltstone reservoir after hydrate decomposition using numerical simulation. One natura extension of this work is to formulate more sophisticated TPG model under much complicated in-situ conditions, such as various temperature, pressure and hydrate saturation.

## CRediT authorship contribution statement

**Cheng Lu**: Conceptualization, Methodology, Resources, Funding acquisition, Supervision. **Xuwen Qin**: Conceptualization, Investigation. **Chao Ma**: Investigation, Software, Writing - original draft, Validation, Formal analysis. **Lu Yu**: Investigation, Software, Data curation, Writing - original draft & review, Validation, Formal analysis. **Lantao Geng**: Methodology, Validation. **Keni Zhang**: Software, Writing – review. **Hang Bian**: Project administration.

## Declaration of Competing Interest

The authors declare that they have no known competing financial interests or personal relationships that could have appeared to influence the work reported in this paper.

## Acknowledgements

The authors are grateful to the National Natural Science Foundation of China (51991365), Key Special Project for Introduced Talents Team of Southern Marine Science and Engineering Guangdong Laboratory (Guangzhou) (GML2019ZD0105) and Key Program of Marine Economy Development (Six Marine Industries) Special Foundation of Department of Natural Resources of Guangdong Province [2021]056. China Geological Survey Project (No. DD20211350).

## References

[1] Sloan ED. Fundamental principles and applications of natural gas hydrates. Nature 2003;426(6964):353-59. https://doi.org/10.1038/nature02135.

[2] Klauda JB, Sandler SI. Global distribution of methane hydrate in ocean sediment. Energy Fuels 2005;19(2):459-70. https://doi.org/10.1021/ef049798o.

[3] Gao Y, Chen M. Evaluation of thermal stimulation in hydrate reservoirs under hot-water cyclic injection. Arabian J Geosci 2020;13:449. https://doi.org/10.1007/s12517-020-05384-w.

[4] Terzariol M, Goldsztein G, Santamarina J. Maximum recoverable gas from hydrate bearing sediments by depressurization. Energy 2017;141:1622-8.
http://dx.doi.org/10.1016/j.energy.2017.11.076.

[5] Sun X, Luo T, Wang L, Wang H, Song Y, Li Y. Numerical simulation of gas recovery from a low-permeability hydrate reservoir by depressurization. Appl Energy 2019;250:7-18.
https://doi.org/10.1016/j.apenergy.2019.05.035.

[6] Qin XW, Liang QY, Ye JL, Yang L, Qiu HJ, Xie WW, et al. The response of temperature and pressure of hydrate reservoirs in the first gas hydrate production test in South China Sea. Appl Energy 2020;278:115649. https://doi.org/10.1016/j.apenergy.2020.115649.

[7] Zhang L, Kuang Y, Zhang X, Song Y, Liu Y, Zhao J. Analyzing the process of gas production from methane hydrate via nitrogen injection. Ind Eng Chem Res 2017;56(26):7585-92. https://doi.org/10.1021/acs.iecr.7b01011.

[8] Wang Y, Sun Z, Li Q, Lv X, Ge Y. A thermal chemical reaction system for natural gas hydrates exploitation. Front Energy Res 2022;9:804498.
https://doi.org/10.3389/fenrg.2021.804498.

[9] Lv J, Cheng Z, Duan J, Wang S, Xue K, Liu Y, et al. Enhanced CH4 recovery from hydrate-bearing sand packs via CO2 replacement assisted thermal stimulation method. J Nat Sci Eng 2021;96:104326. https://doi.org/10.1016/j.jngse.2021.104326.

[10] Hassanpouryouzband A, Joonaki E, Farahani MV, Takeya S, Ruppel C, Yang JH, et al. Gas Hydrates in sustainable chemistry. Chem Soc Rev 2020;49(4): 5225-309.
https://doi.org/10.1039/c8cs00989a.

[11] Song Y, Yang L, Zhao J, Liu W, Yang M, Li Y. The status of natural gas hydrate research in China: a review. Renew Sust Energ Rev 2014;31:778–91.
https://doi.org/10.1016/j.rser.2013.12.025

[12] Hassanpouryouzband A, Yang JH, Tohidi B, Chuvilin E, Istomin V, Bukhanov B, et al. $CO_2$ capture by injection of flue gas or $CO_2$-$N_2$ mixtures into hydrate reservoirs: Dependence of $CO_2$ capture efficiency on gas hydrate reservoir conditions. Enviro Sci Tech 2018;52(7):4324-30.
https://doi.org/10.1021/acs.est.7b05784.

[13] Li JF, Ye JL, Qin XW, Qiu HJ, Wu NY, Lu HL, et al. The first offshore natural gas hydrate production test in South China Sea. China Geol 2018;1(1):5-16.
https://doi.org/10.31035/cg2018003.

[14] Ye JL, Qin XW, Xie WW, Lu HL, Ma BJ, Qiu HJ, et al. Main progress of the second gas hydrate trial production in the South China Sea. China Geol 2020;47(3):557-68. (in Chinese).
https://doi.org/10.12029/gc20200301.

[15] Moridis GJ, Collett TS, Pooladi-Darvish M, Hancock S, Santamarinaet C, Boswell R, et al. Challenges, uncertainties, and issues facing gas production from gas-hydrate deposits. SPE

660 Reserv Eval Eng 2011;14(01):76-112. https://doi.org/10.2118/131792-PA.
661 [16] Wu NY, Zhang HQ, Yang SX, Zhang GX, Liang JQ, Lu JA, et al. Gas Hydrate System
662 of Shenhu Area, Northern South China Sea: Geochemical Results. J Geol Res 2011;370298.
663 https://doi.org/10.1155/2011/370298.
664 [17] Liu CL, Ye YG, Meng QG, He HL, Lu HL, Zhang J, et al. The characteristics of gas
665 hydrates recovered from Shenhu area in the South China Sea. Mar Geol 2012;307-310:22-7.
666 https://doi.org/10.1016/j.margeo.2012.03.004.
667 [18] Yang SX, Zhang HQ, Wu NY, Su X, Schultheiss P, Holland M, et al. High concentration
668 hydrate in disseminated forms obtained in Shenhu area, north slope of south China sea. In:
669 Proceedings of 6th ICGH, Vancouver, British Columbia, Canada;2008.
670 http://hdl.handle.net/2429/1178.
671 [19] Chen F, Zhou Y, Su X, Liu GH, Lu HF, Wang JL. Gas hydrate saturation and its relation
672 with grain size of the hydrate-bearing sediments in the Shenhu Area of northern South China Sea.
673 Mar Geol Quat Geol 2011;31(5):95-100. (in Chinese).
674 https://doi.org/10.3724/SP.J.1140.2011.05095.
675 [20] Chen F, Su X, Lu HF, Zhou Y, Zhuang C. Relations between biogenic component and
676 highly saturated gas hydrate distribution from Shenhu Area, northern South China Sea. J Earth Sci
677 2012;38(5):907-15. (in Chinese). https://doi.org/10.3799/dqkx.2013.089.
678 [21] Liu CL, Meng QG, Li CF, Sun JY, He XL, Yang SX, et al. Characterization of natural
679 gas hydrate and its deposits recovered from the northern slope of the South China Sea. Front Earth
680 Sci 2017;24(4):41-50. (in Chinese). https://doi.org/10.13745/j.esf.yx.2016-12-35.
681 [22] Chen ZY, Zhou JX, Wang HJ. Soil Mechanics. Beijing: Tsinghua Univ Press;1994. (in
682 Chinese).
683 [23] Mithcell JK. Fundamentals of soil behavior. New York: Wiley;1976.
684 [24] Gu RG, Fang YG. Experimental research on ion effects of ultrafine granular clay
685 seepage. Rock Soil Mec 2009;30(6):1595-603. (in Chinese).
686 https://doi.org/10.16285/j.rsm.2009.06.044.
687 [25] Prada A, Civan F. Modification of Darcy's law for the threshold pressure gradient. J Pet
688 Sci Eng 1999;22(4):237-40. https://doi.org/10.1016/S0920-4105(98)00083-7.
689 [26] Miller RJ, Low PF. Threshold Gradient for Water Flow in Clay Systems. Soil Sci Soc
690 Am J 1963;27(6):605-12. https://doi.org/10.2136/sssaj1963.03615995002700060013x.
691 [27] Wu D, Brantson ET, Ju B. Numerical simulation of water alternating gas flooding (wag)
692 using co2 for high-salt argillaceous dolomite reservoir considering the impact of stress sensitivity
693 and threshold pressure gradient. Acta Geophysica, 2021;69:1349-65.
694 https://doi.org/10.1007/s11600-021-00601-w.
695 [28] Wang R, Yang J, Wang M, Zhao Y, Chen W. Effect of threshold pressure gradients on
696 control areas determination of production well in CBM reservoirs. Advanc Polymer Tech
697 2019;3517642. https://doi.org/10.1155/2019/3517642.
698 [29] Ren S, Shen F, Yang S, Zhang X, Luo H, Feng C. Analysis and calculation of threshold
699 pressure gradient based on capillary bundle. Math Prob Eng 2021;5559131.
700 https://doi.org/10.1155/2021/5559131.
701 [30] Liu WG, Wu ZR, Li JJ, Zhen JN, Li YH. The seepage characteristics of methane

hydrate-bearing clayey sediments under various pressure gradients. Energy 2020;191:16507. https://doi.org/10.1016/j.energy.2019.116507.

[31] Zhao YZ, Cheng YF, Liu YC, Sun DX, Du P. Study on influence of start-up pressure gradient to micro-seepage in low permeability reservoirs and development trends. Pet Geol Recov Effic 2013;20(1):67-9. (in Chinese). https://doi.org/10.13673/j.cnki.cn37-1359/te.2013.01.017.

[32] Ning B, Xiang ZP, Liu XS, Li ZJ, Chen ZH, Jiang BC, et al. Production prediction method of horizontal wells in tight gas reservoirs considering threshold pressure gradient and stress sensitivity. J Pet Sci Eng 2020;187:106750. https://doi.org/10.1016/j.petrol.2019.106750.

[33] Yu L, Zhang L, Zhang R, Ren SR. Assessment of natural gas production from hydrate-bearing sediments with unconsolidated argillaceous siltstones via a controlled sandout method. Energy 2018;160:654-67. https://doi.org/10.1016/j.energy.2018.07.050.

[34] Zhao EM, Hou J, Liu YG, Ji YK, Liu WB, Lu N, et al. Enhanced gas production by forming artificial impermeable barriers from unconfined hydrate deposits in Shenhu area of South China sea. Energy 2020;213:118826. https://doi.org/10.1016/j.energy.2020.118826.

[35] Li G, Moridis GJ, Zhang KN, Li XS. The use of huff and puff method in a single horizontal well in gas production from marine gas hydrate deposits in the Shenhu Area of South China Sea. J Pet Sci Eng 2011;77(1):49-68. https://doi.org/10.1016/j.petrol.2011.02.009.

[36] Cai JC, Xia YX, Lu C, Bian H, Zou SM. Creeping microstructure and fractal permeability model of natural gas hydrate reservoir. Mar Petrol Geol 2020;115:104282. https://doi.org/10.1016/j.marpetgeo.2020.104282.

[37] Li YL, Liu, LL, Jin YR. Wu NY. Characterization and development of natural gas hydrate in marine clayey-silt reservoirs: A review and discussion. Adv Geo-Energy Res 2021;5(1):75-86. https://doi.org/10.46690/ager.2021.01.08.

[38] Sun YH, Ma XL, Guo W, Jia R, Li B. Numerical simulation of the short- and long-term production behavior of the first offshore gas hydrate production test in the South China Sea. J Pet Sci Eng 2019;181:106196. https://doi.org/10.1016/j.petrol.2019.106196.

[39] Yang L, Ye JL, Qin XW, Liang QY, Wu XM. Effects of the seepage capability of overlying and underlying strata of marine hydrate system on depressurization-induced hydrate production behaviors by horizontal well. Mar Pet Geol 2021;128:105019. https://doi.org/10.1016/j.marpetgeo.2021.105019.

[40] Moridis G.J., Kowalsky M.B., Pruess K. TOUGH-Fx/HYDRATE v1.0 User's Manual: A code for the Simulation of System Behavior in Hydrate-Bearing Geologic Media. Report LBNL-58950, Lawrence Berkeley National Laboratory, Berkeley, California;2014.

[41] Thomas KL, Katz DL, Tek MR. Threshold pressure phenomena in porous media. SPE J 1967;8(02):174 -84. https://doi.org/10.2118/1816-PA.

[42] Li ZX, Han HB, Cheng LS, Zhang ML, Shi CE. A new solution and application of starting pressure gradient in ultra-low permeability reservoir. Pet Explor Dev 2004;31(3):107-09. (in Chinese). https://doi.org/10.3321/j.issn:1000-0747.2004.03.029.

[43] Bear J. Dynamic of fluid in porous media. New York: American Elsevier Publishing Company, Inc; 1972.

[44] Dai YD, Pang X. Petroleum geological characteristics of Zhu II depression, Pearl River Mouth Basin. China Offshore Oil and Gas 1999;13(3):169-73. (in Chinese).

[45] Huang L, Su Z, Wu NY. Evaluation on the gas production potential of different lithological hydrate accumulations in marine environment. Energy 2015;91:782-87. https://doi.org/10.1016/j.energy.2015.08.092.

[46] Mao PX, Sun JX, Ning FL, Hu GW, Wan YZ, Cao XX, et al. Effect of permeability anisotropy on depressurization induced gas production from hydrate reservoirs in the South China Sea. Energy Sci Eng 2020;8(8):2690-707. https://doi.org/10.1002/ese3.701.

[47] Wu NY, Yang SX, Zhang HQ, Liang JQ, Wang HB, Su X, et al. Preliminary discussion on gas hydrate reservoir system of Shenhu Area, North Slope of South China Sea. In: Proceedings of the 6th International conference on gas hydrates, Vancouver, British Columbia, Canada;2008.

[48] Van Genuchten MT. A closed-form equation for predicting the hydraulic conductivity of unsaturated soils. Soil Sci Soc Am J 1980;44(5):892-98. https://doi.org/10.2136/sssaj1980.03615995004400050002x.

[49] Stone HL. Probability model for estimating three-phase relative permeability. J Pet Tech 1970;22(2):214-18. https://doi.org/10.2118/2116-PA.

[50] Yu MH, Li WZ, Jiang LL, Wang X, Yang MJ, Song YC. Numerical study of gas production from methane hydrate deposits by depressurization at 274 K. Appl Energy 2018;227:28-37. https://doi.org/10.1016/j.apenergy.2017.10.013

[51] Li SX, Wang ZQ, Li S, Wang XP, Hao YM. Investigations on performance of hydrate dissociation by depressurization near the quadruple point. J Nat Gas Sci Eng 2021;103929. https://doi.org/10.1016/j.jngse.2021.103929

[52] Lu C, Wang JH, Zhang C, Cheng MH, Wang XD, Dong WX, et al. Transient pressure analysis of a volume fracturing well in fractured tight oil reservoirs. J Geophys Eng 2017;14(6):1509-20. https://doi.org/10.1088/1742-2140/aa8115.